

Supplementary Information

Demixing the miscible liquids: Toward biphasic battery electrolytes based on the kosmotropic effect

Won-Yeong Kim^{1,†}, Hong-I Kim^{2,†}, Kyung Min Lee^{2,†}, Eunhye Shin², Xu Liu^{3,4}, Hyunseok Moon¹, Henry Adenusi⁵, Stefano Passerini^{3,4,*}, Sang Kyu Kwak^{2,*} and Sang-Young Lee^{1,6,*}

¹Department of Chemical and Biomolecular Engineering, Yonsei University, 50 Yonsei-ro, Seodaemun-gu, Seoul 120-749, Republic of Korea

²Department of Energy Engineering, School of Energy and Chemical Engineering, Ulsan National Institute of Science and Technology (UNIST), Ulsan 44919, Republic of Korea

³Helmholtz Institute Ulm (HIU), Helmholtzstraße 11, 89081, Ulm, Germany

⁴Karlsruhe Institute of Technology (KIT), P.O. Box 3640 D-76021, Karlsruhe, Germany

⁵Hong Kong Quantum AI Lab (HKQAI), 17 Science Park West Avenue, Hong Kong 999077, China

⁶Lead Contact

†These authors contributed equally.

*Correspondence: syleek@yonsei.ac.kr, skkwak@unist.ac.kr, stefano.passerini@kit.edu

Supplementary Figures

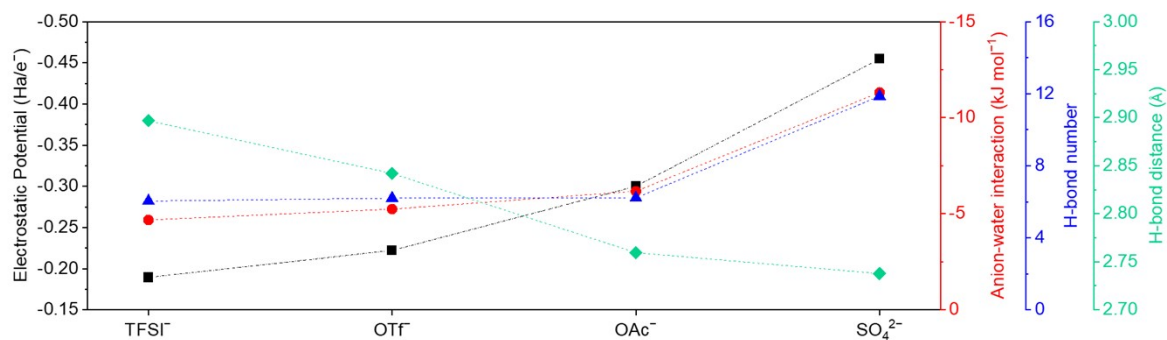


Figure S1. Relationship between electrostatic potential and water structure in various kinds of anions. The anion-water interaction energy, H-bond number (normalized by the number of water molecules) and H-bond distance was calculated from the MD trajectories.

The stronger kosmotropic anion (e.g., SO_4^{2-}) tends to show the larger H-bond number (representing the number of hydrogen bonds between water and anion) and smaller H-bond distance.

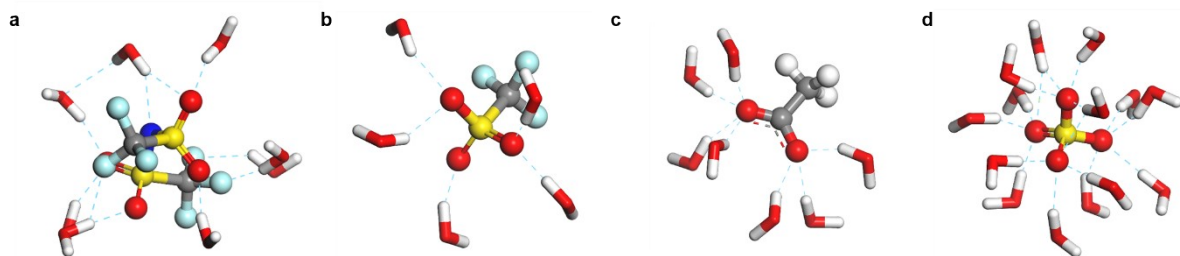


Figure S2. Hydration structure of anions. (a) TFSI⁻, (b) OTf⁻, (c) OAc⁻, and (d) SO₄²⁻. Gray, blue, white, red, yellow, cyan balls represent carbon, nitrogen, hydrogen, oxygen, sulfur, fluorine, respectively.

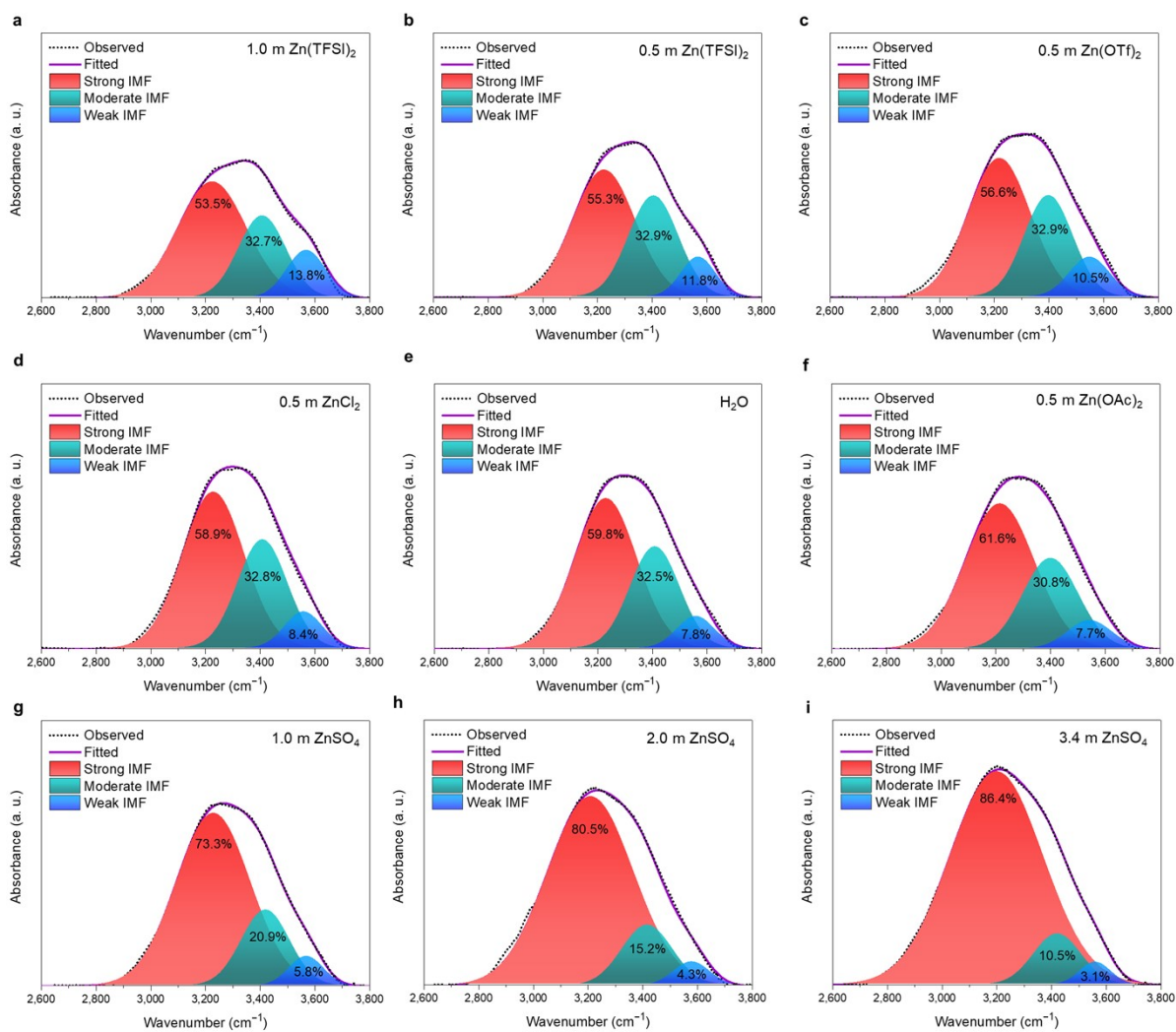


Figure S3. Peak-fitting of the FTIR O–H stretching vibration in various aqueous electrolytes. (a) 1.0 m Zn(TFSI)₂, (b) 0.5 m Zn(TFSI)₂, (c) 0.5 m Zn(OTf)₂, (d) 0.5 m ZnCl₂, (e) H₂O, (f) 0.5 m Zn(OAc)₂, (g) 1.0 m ZnSO₄, (h) 2.0 m ZnSO₄, and (i) 3.4 m ZnSO₄.

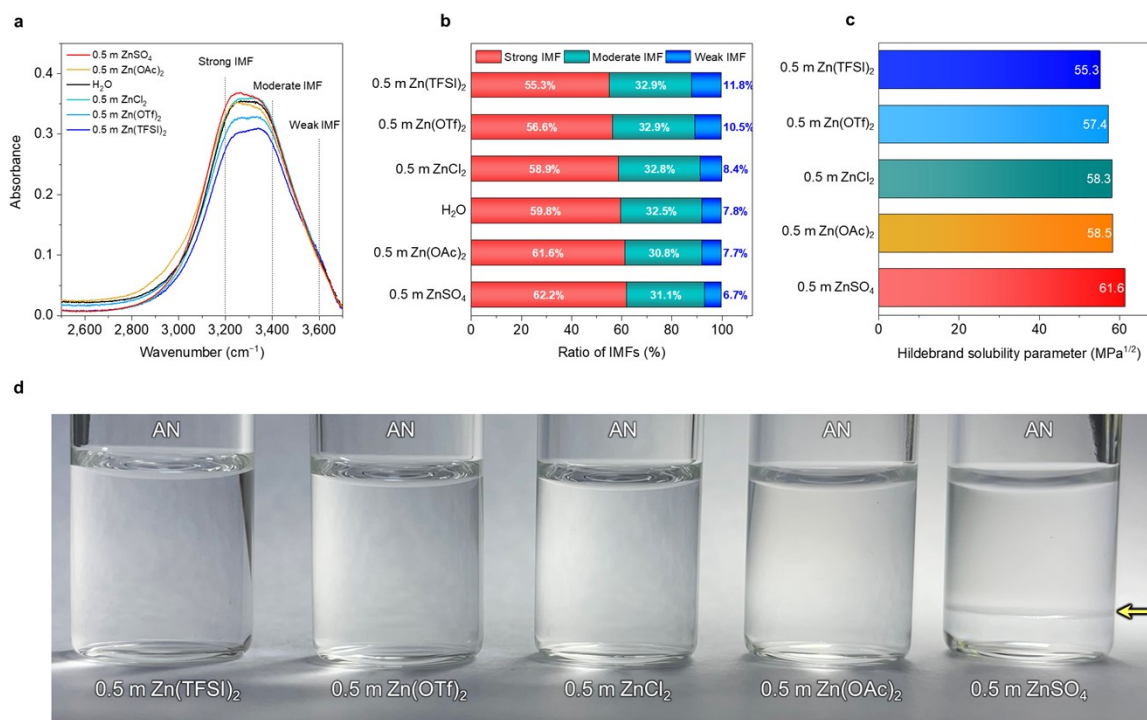


Figure S4. Effects of kosmotropic/chaotropic anions on electrolyte structure at a low salt concentration of 0.5 m. (a) FTIR spectra of various aqueous electrolytes as a function of anion species. (b) Comparison in the relative portion of the three (strong, moderate, and weak) IMFs obtained from O–H stretching bands in the FTIR spectra. (c) Hildebrand solubility parameter (δ) values of the electrolytes calculated from the MD trajectory. (d) Photograph of various aqueous electrolytes/AN (1/1, v/v) mixtures at ambient temperature.

The FTIR spectra of the aqueous electrolytes showed the higher absorbance of strong IMF and lower absorbance of weak IMF as the kosmotropic effect increased (**Figure S4a**). These results were quantitatively verified by analyzing the relative portion of three IMFs in the O–H stretching bands (**Figure S4b**) and Hildebrand solubility parameter (δ) values calculated by the MD trajectory (**Figure S4c**). When AN (a polar nonaqueous solvent that is miscible with pure water) was coupled with these aqueous electrolytes, only 0.5 m ZnSO₄ showed the phase separation with AN despite the lower anion concentration (one half of those of the other salts) (**Figure S4d**). This result confirms the kosmotropic effect of ZnSO₄ on the phase separation with AN.

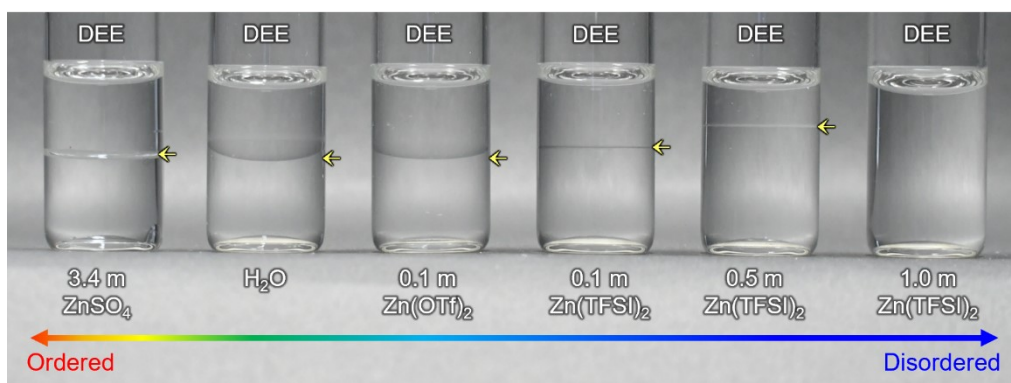


Figure S5. Photograph of various aqueous electrolyte/DEE (1/1, v/v) mixtures at ambient temperature.

Diethyl ether (DEE), which is immiscible with water, was mixed with various aqueous electrolytes. An aqueous electrolyte of 3.4 m ZnSO_4 was phase-separated from DEE because of the ordered structure enabled by kosmotropic SO_4^{2-} . Meanwhile, an aqueous electrolyte of 0.1 m $\text{Zn}(\text{OTf})_2$ was immiscible with DEE, revealing insufficient structure-breaking ability of the relatively weak chaotropic OTf^- . For TFSI^- , which is a stronger chaotropic anion than OTf^- , positions of DEE-aqueous electrolyte interfaces moved upward with increasing salt ($\text{Zn}(\text{TFSI})_2$) concentration from 0.1 to 0.5 m. Eventually, an aqueous electrolyte of 1.0 m $\text{Zn}(\text{TFSI})_2$ was miscible with DEE, in which the DEE can strongly interact with water due to the weakened water-water interaction achieved by the strong chaotropic TFSI^- .

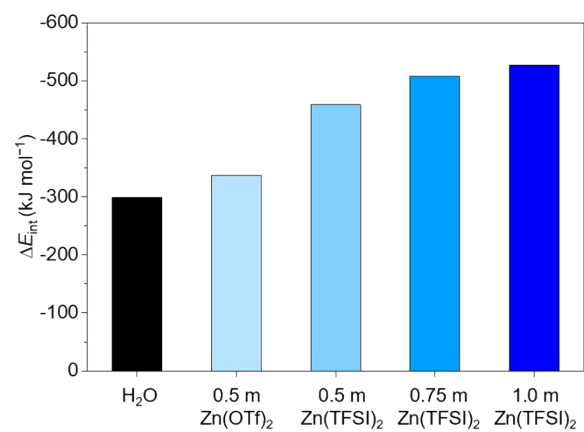


Figure S6. Average interaction energy (ΔE_{int} , normalized by the number of water molecule) between aqueous electrolytes and DEE. ΔE_{int} was obtained by averaging the interaction energies of the MD trajectories from 4 ns to 5 ns.

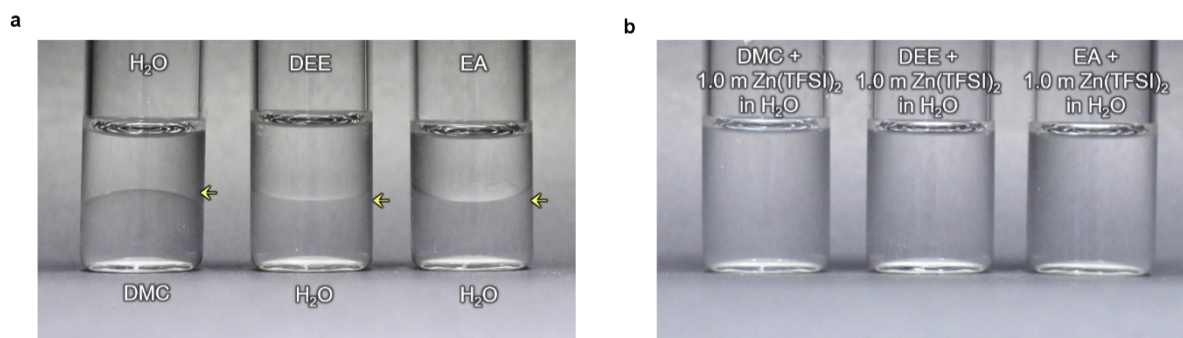


Figure S7. (a and b) Photographs of mixtures between nonaqueous solvents and pure water (a), and 1.0 m Zn(TFSI)₂ in H₂O (b).

Dimethyl carbonate (DMC) and ethyl acetate (EA), which are intrinsically immiscible with water, were mixed with a disordered aqueous electrolyte of 1.0 m Zn(TFSI)₂. In contrast to the pure water, the disordered aqueous electrolyte of 1.0 m Zn(TFSI)₂ showed good miscibility with the DMC and EA. This result indicates that water molecules in the disordered aqueous electrolyte could easily interact with the DMC and EA, verifying the role of chaotropic anion (TFSI⁻).

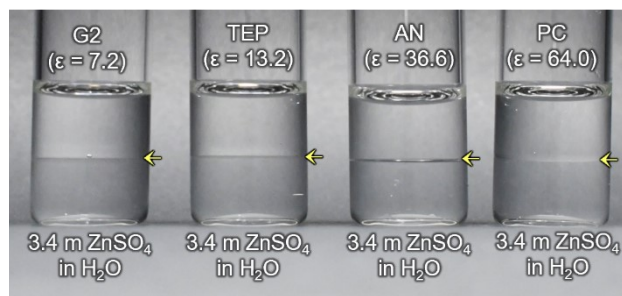


Figure S8. Photograph of mixtures (nonaqueous solvent/3.4 m ZnSO₄ in H₂O = 1/1 (v/v)).

Trimethyl phosphate (TEP), diglyme (G2), and propylene carbonate (PC), which are intrinsically miscible with water, were mixed with an ordered aqueous electrolyte of 3.4 m ZnSO₄. The TEP, G2, and PC were not miscible with the aqueous electrolyte of 3.4 m ZnSO₄, exhibiting the viable role of kosmotropic anion (SO₄²⁻) in modulating the phase separation behavior.

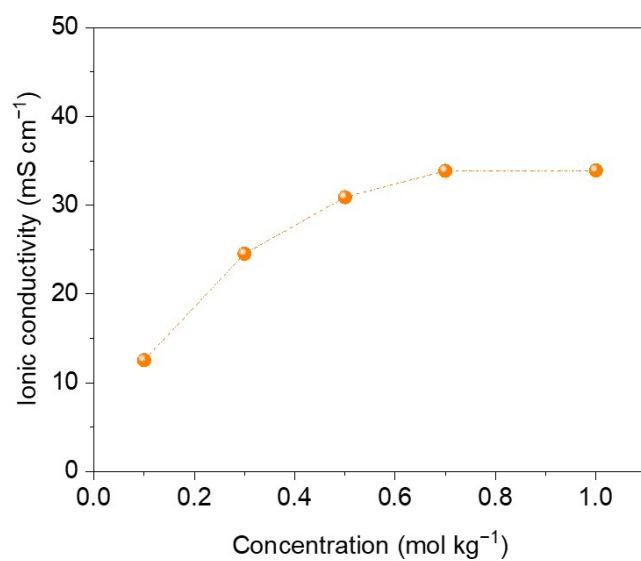


Figure S9. Ionic conductivity of the nonaqueous electrolytes ($\text{Zn}(\text{TFSI})_2$ in AN) at different concentrations.

The ionic conductivity of the nonaqueous electrolytes tends to increase with $\text{Zn}(\text{TFSI})_2$ concentration and then was equilibrated over the concentration of 0.5 m.

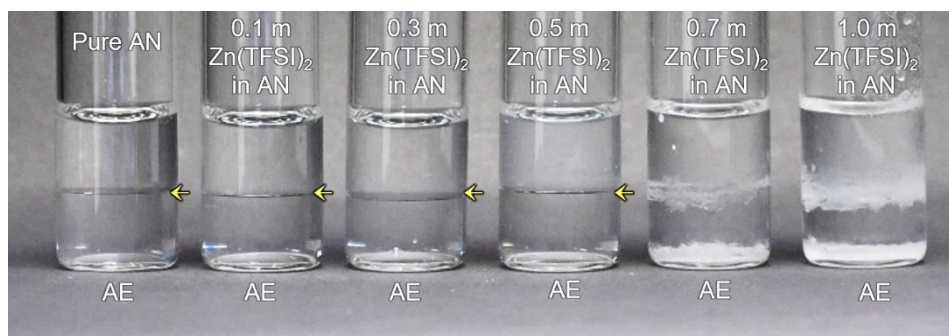


Figure S10. Photographs of the mixture between AE and nonaqueous electrolytes ($\text{Zn}(\text{TFSI})_2$ in AN) at different concentrations.

The nonaqueous electrolytes maintained the phase separation with the AE up to the $\text{Zn}(\text{TFSI})_2$ concentration of 0.5 m. Further increase of the concentration resulted in the precipitation of the $\text{Zn}(\text{TFSI})_2$ salt.

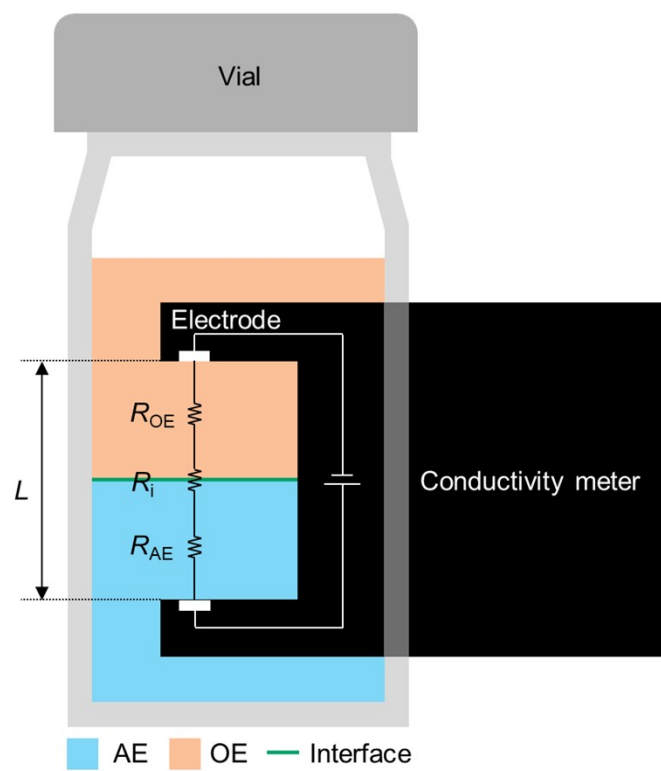


Figure S11. Schematic of the conductivity meter used to measure the ionic conductivity of the BLE.

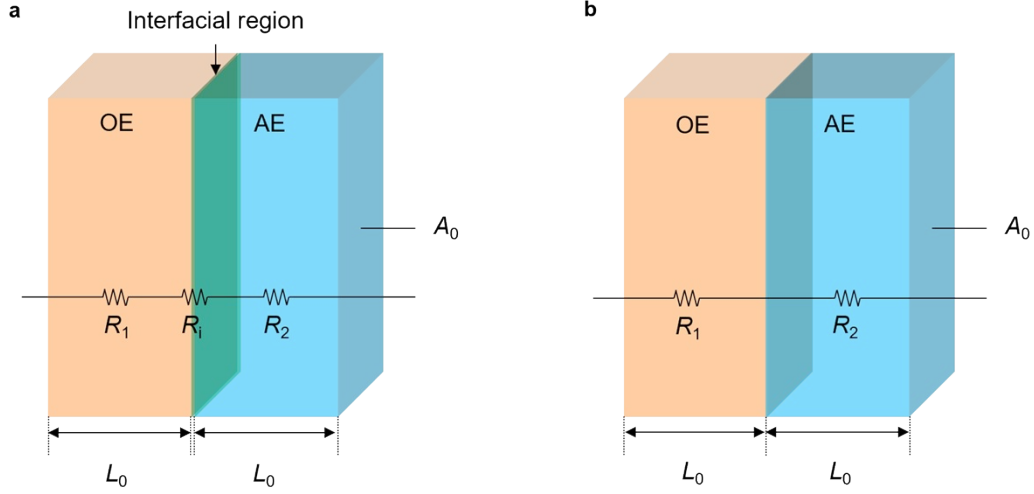


Figure S12. Schematic representation of the BLE system (a) with interfacial region between two different electrolytes and (b) that assumes no liquid/liquid interface resistance.

Total resistance for ion conduction in the BLE is the sum of two resistances of single-phase electrolyte (R_1 and R_2) and an interfacial resistance (R_i) as described in **Figure S12a**. To investigate the ion conduction through the liquid/liquid interface in the BLE, modeling of the hypothetical BLE system without R_i is described in **Figure S12b**. The hypothetical ionic conductivity (σ_4) of BLE without interfacial resistance can be estimated based on the relationships in the series of equations. Resistivity, which means resistance of a conductor of unit cross-sectional area and unit length, is expressed by equation (1).

$$R = \frac{\rho L}{A} \quad (1)$$

where, R is resistance, ρ is resistivity, L is distance, A is area, respectively. Ionic conductivity (σ) of electrolytes, which is the reciprocal of resistivity, is calculated in equation (2).

$$\sigma = \frac{1}{\rho} = \frac{L}{RA} \quad (2)$$

As shown in **Figure S12b**, total resistance is the sum of the two resistances of single-phase electrolytes connected in-series (R_1 and R_2). Also, each electrolyte phases have length of L_0 with an area of A_0 . Therefore, the ionic conductivity of the BLE that assumes no resistance at the interfacial region (σ_4) can be derived in equation (3) from combining equation (1) and equation (2).

$$\sigma_4 = \frac{2L_0}{(R_1 + R_2)A_0} = \frac{2L_0}{\left(\frac{\rho_1 L_0}{A_0} + \frac{\rho_2 L_0}{A_0}\right)A_0} = \frac{2}{(\rho_1 + \rho_2)} = \frac{2}{\left(\frac{1}{\sigma_1} + \frac{1}{\sigma_2}\right)} \quad (3)$$

Based on the experimental data of the single-phase electrolytes of the OE (σ_1) and the AE (σ_2) at various temperatures, σ_4 was estimated and compared with measured ionic conductivity of the BLE (σ_3) in **Table S5** and plotted in **Figure 4b**.

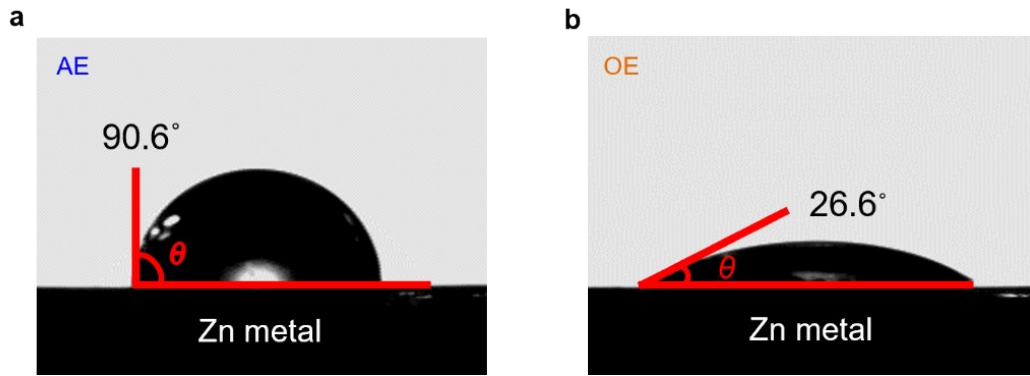


Figure S13. Contact angle against the Zn metal anode. (a) AE, (b) OE.

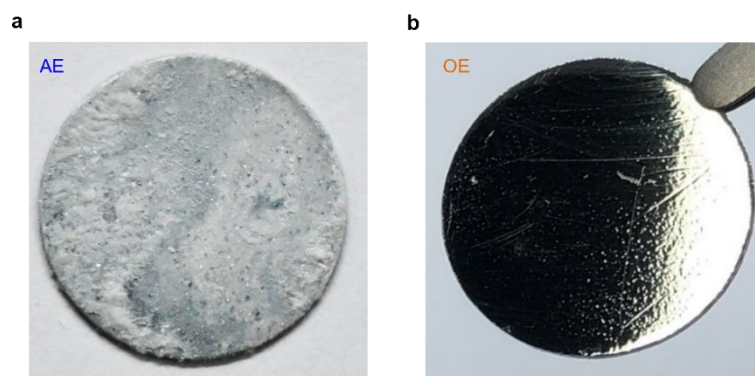


Figure S14. Photographs of Zn metal after immersing Zn in (a) AE and (b) OE for 7 days.

Even after being soaked into the OE for 7 days, the Zn metal remained almost unchanged and the surface remained smooth, whereas the Zn metal soaked in the AE became white and roughened together with scattered flakes, disclosing the formation of byproducts mostly stemming from Zn corrosion.

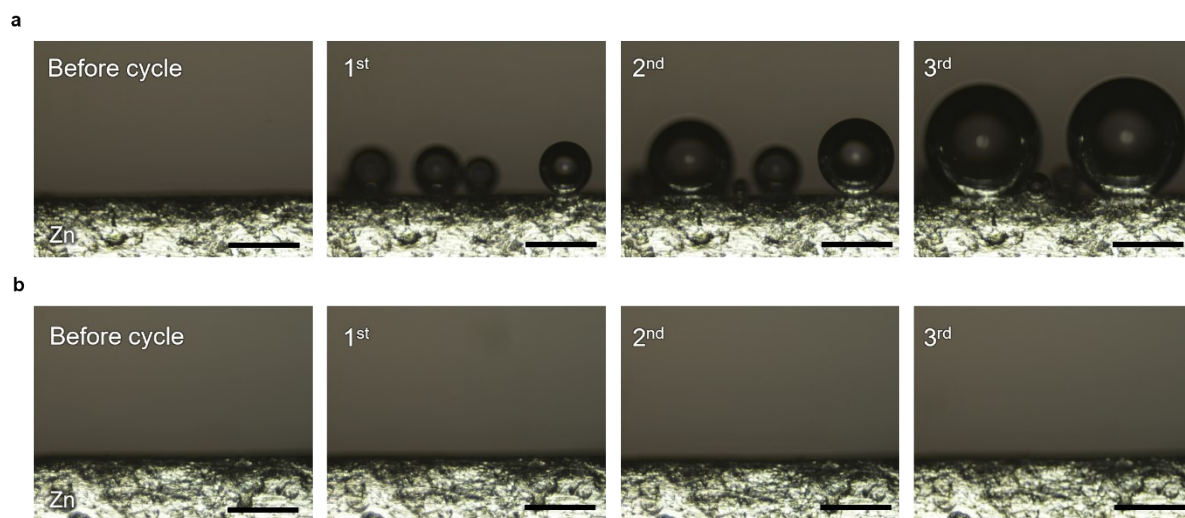


Figure S15. *In situ* optical microscopic images of the Zn metals during Zn plating/stripping in (a) AE and (b) OE at current density of 5 mA cm^{-2} with the areal capacity of 5 mAh cm^{-2} . Scale bar, $200 \text{ }\mu\text{m}$.

The electrochemical stability of Zn metals with AE and OE was examined by monitoring their surface change during Zn plating/stripping using *in situ* optical microscopy. For the AE, gas bubbles were vigorously generated on the Zn metal, which could expedite uneven and random Zn deposition. In contrast, no gas bubble was observed on the Zn metal cycled in the OE, exhibiting good electrochemical stability between the OE and Zn metal.

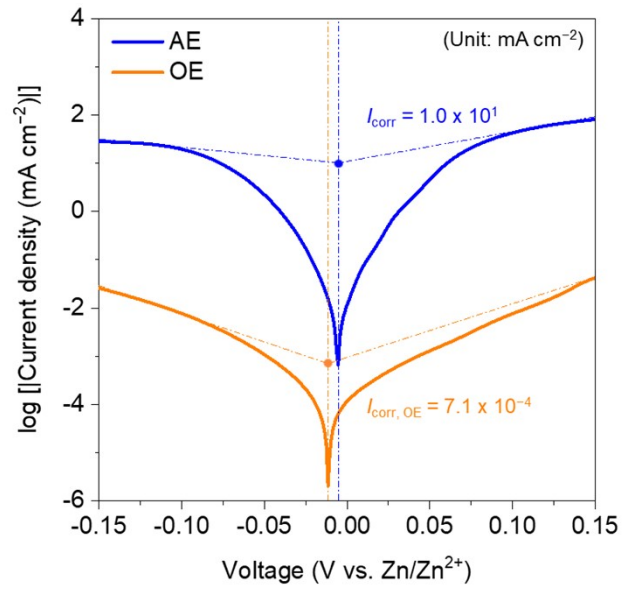


Figure S16. Tafel plots of the Zn metal in contact with the AE and OE.

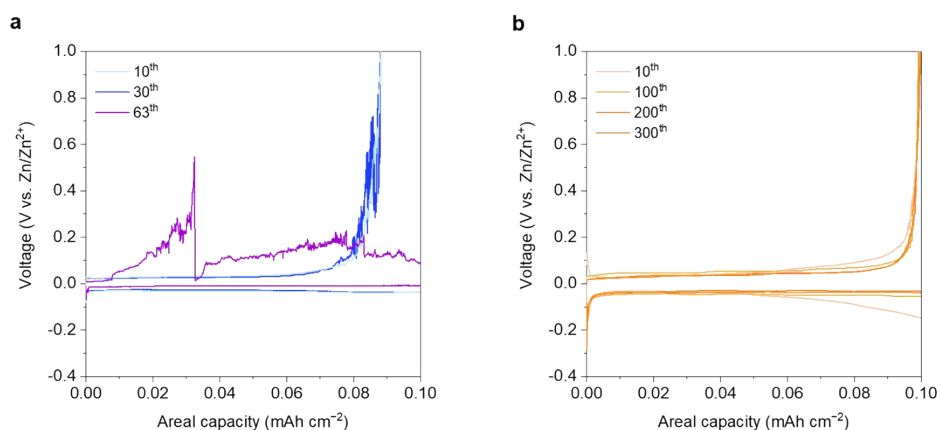


Figure S17. Galvanostatic Zn plating/stripping profiles of the Zn||Ti cells at a current density of 0.1 mA cm⁻² with areal capacity of 0.1 mAh cm⁻² in (a) AE and (b) OE.

The CEs of the cell employing the AE were lower than 90% and highly fluctuated after 20 cycles, revealing the parasitic side reactions, Zn dendrite growth, and formation of dead Zn. After 63 cycles, the cell failed to operate due to the occurrence of internal short-circuit. By comparison, a cell employing the OE displayed a high CE of 99.6 % even after 300 cycles, indicating for a superior reversibility of Zn plating/stripping in the OE.

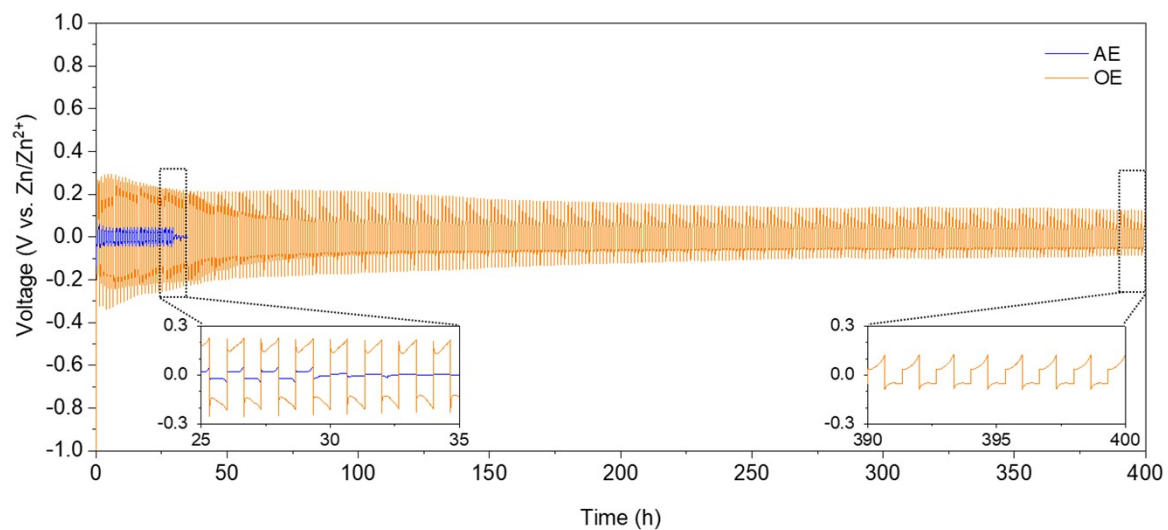


Figure S18. Voltage profiles of Zn||Zn symmetric cells with AE and OE at an areal current density of 1.5 mA cm^{-2} and an areal capacity of 1 mAh cm^{-2} .

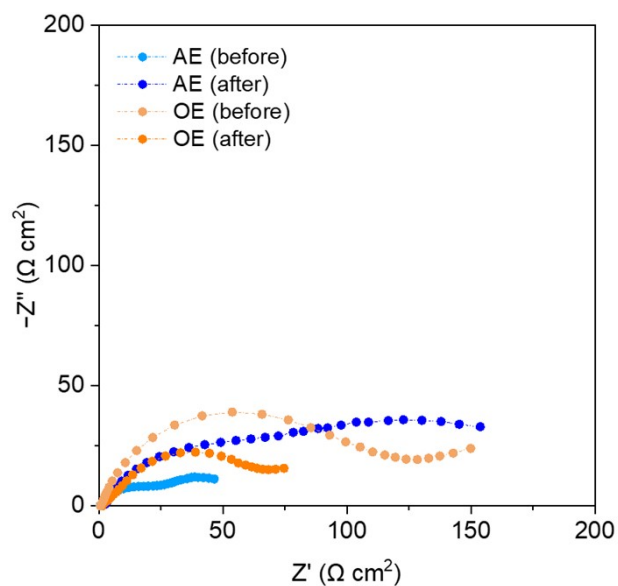


Figure S19. EIS profiles of Zn||Zn symmetric cells before and after the cycling test at a current density of 1.5 mA cm^{-2} and an areal capacity of 1 mAh cm^{-2} .

The cell with AE showed the relatively lower impedance than the cell with OE before the cycling test. However, the impedance of the cell with AE was significantly increased after the cycling test mainly due to the formation of resistive byproducts stemming from interfacial parasitic side reactions. By comparison, the cell with OE showed a slight decrease in the impedance after the cycling test, which was consistent with the voltage profiles of Zn||Zn symmetric cells shown in **Figure S18**.

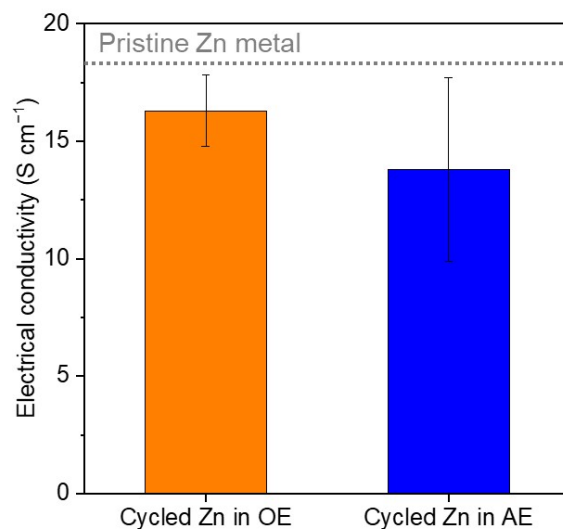


Figure S20. Electrical conductivities of the cycled Zn metal electrodes in contact with OE and AE after 100 cycles. Gray dotted-line indicates an electrical conductivity of a pristine Zn metal electrode (18.2 S m⁻¹) before the cycling test.

The cycled Zn metal electrode in contact with OE showed the higher electrical conductivity with small standard deviation (OE: 16.3 ± 1.5 S m⁻¹) compared to that of the cycled Zn metal electrode in contact with AE (AE: 13.8 ± 3.9 S m⁻¹). This result exhibits that the electrically active surface of the Zn metal electrode in contact with OE was not seriously contaminated after the cycling test.

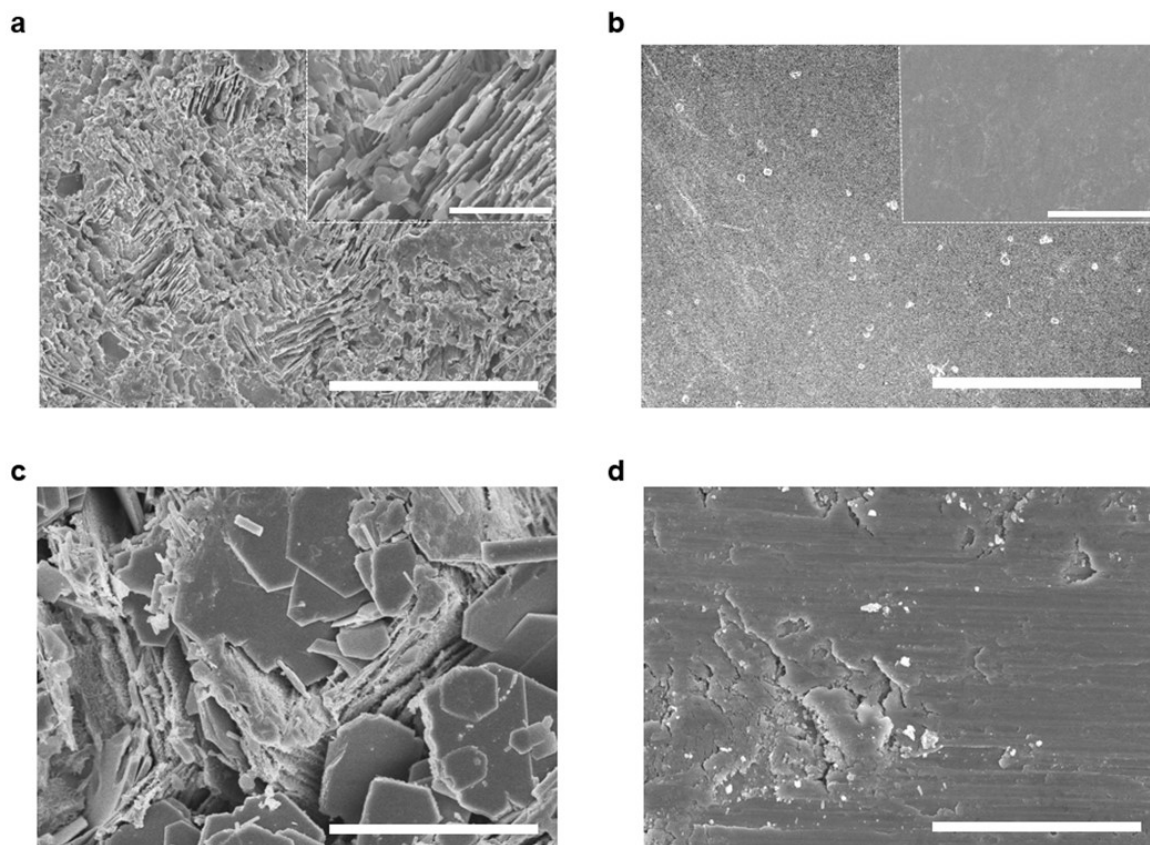


Figure S21. SEM images of Zn metal after cycling at a current density of 0.1 mA cm^{-2} and areal capacity of 0.1 mAh cm^{-2} in (a) AE and (b) OE. SEM image of Zn metal after cycling at a current density of 1.5 mA cm^{-2} and areal capacity of 1 mAh cm^{-2} in (c) AE and (d) OE. Scale bars, $10 \mu\text{m}$ (a, b). Scale bars, $100 \mu\text{m}$ (a, b), $10 \mu\text{m}$ (inset of a, b) and $10 \mu\text{m}$ (c, d).

A smooth and uniform surface was formed on the Zn cycled in the OE, whereas the Zn dendrites were randomly distributed and agglomerated on the Zn cycled in the AE.

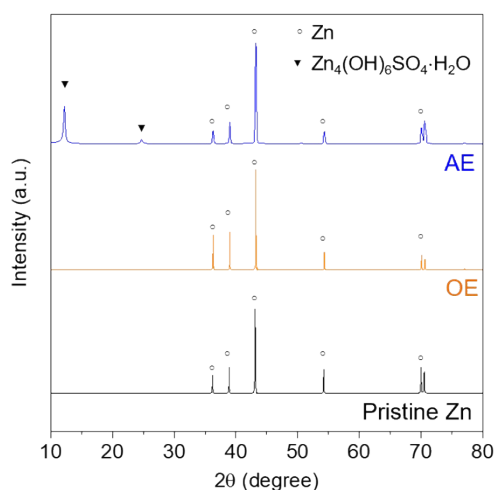


Figure S22. XRD patterns of Zn metal after 100 cycles in AE and OE at a current density of 0.1 mA cm⁻² and areal capacity of 0.1 mAh cm⁻².

The XRD patterns of the Zn cycled in the OE appeared similar to those of the pristine Zn, indicating the electrochemical reversibility during the Zn plating/stripping. By comparison, new crystalline phases with sharp peaks at 12.2° and 24.6° were evolved on the Zn cycled in the AE, which is attributed to the formation of byproducts such as Zn₄SO₄(OH)₆·H₂O.¹

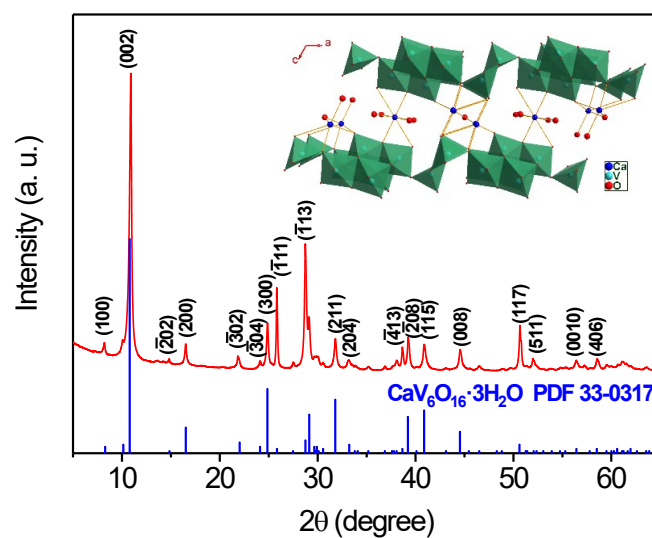


Figure S23. XRD patterns of the synthesized CVO cathode materials.

All the peaks can be indexed to the standard diffraction lines of CVO (PDF 33-0317), whose structure is depicted in the inset. Based on the (002) plane, the calculated interlayer distance was 8.1 Å, which is beneficial for the insertion/extraction of Zn^{2+} ions.

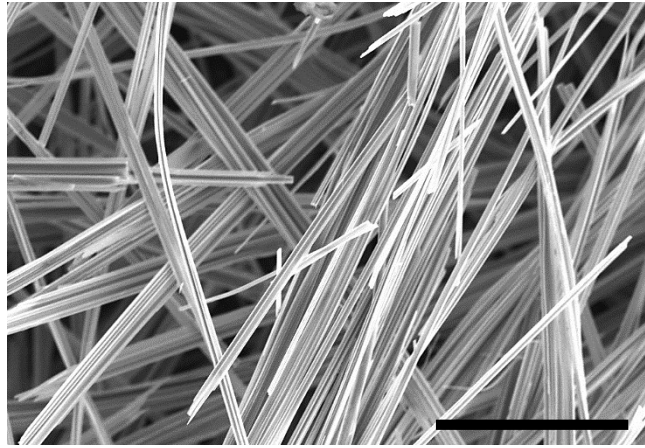


Figure S24. SEM image of the synthesized CVO. Scale bar, 5 μm .

The synthesized CVO was composed of uniform wires longer than tens of micrometers and with a diameter in the range of hundreds of nanometers.

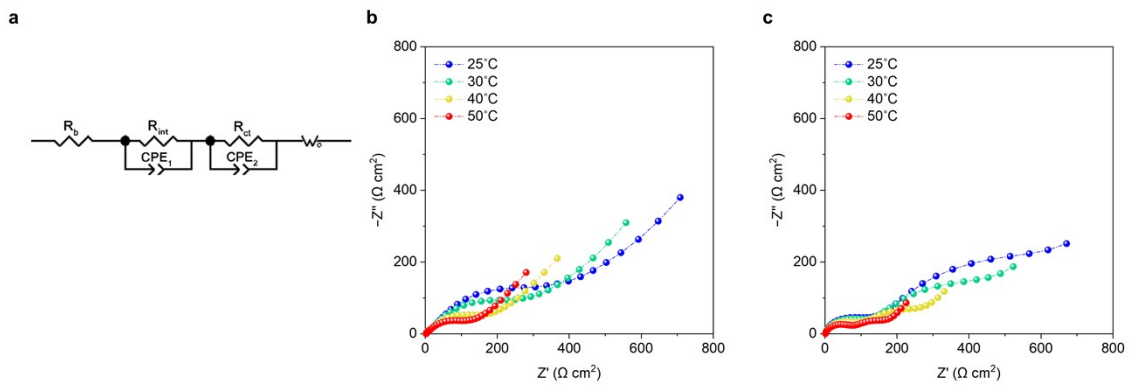


Figure S25. (a) Electrical circuit of Zn_xCVO (SOC 50%) symmetric cells. (b and c) EIS analysis of Zn_xCVO symmetric cells with AE (b) and OE (c) at varying temperature from 25 °C to 50 °C.

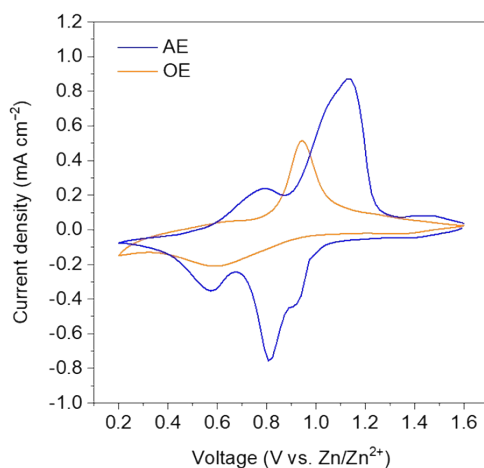


Figure S26. CV profiles of Zn||CVO cells with AE and OE.

The Zn||CVO cells with the AE or OE were analyzed. For the cell with the AE, two sharp redox pairs (i.e., reduction peak at 0.59 V and 0.81 V, oxidation peaks at 0.79 V and 1.12 V) were observed, which appeared similar to a multi-step process of Zn^{2+} insertion/extraction in the previous study.² By contrast, the Zn||CVO cell with the OE showed just one broad redox pair (i.e., reduction peak at 0.60 V and oxidation peak at 0.95 V) with lower current density, revealing sluggish kinetics³ of Zn^{2+} insertion/extraction in the CVO cathode. These results demonstrate that the AE can facilitate both Zn^{2+} diffusion and charge transfer reaction kinetics owing to the formation of facile ion conduction pathways from the bulk electrolyte to the CVO cathode.

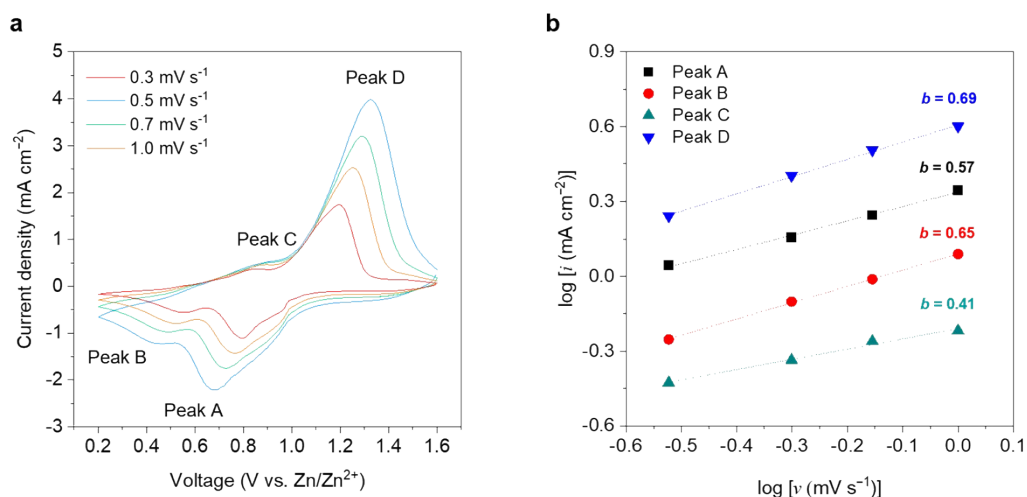


Figure S27. (a) CV profiles of Zn||CVO cells with the BLE at different scan rate from 0.1 to 1.0 mV s⁻¹. (b) Corresponding log (*i*) versus log (*v*) plots of each redox peaks from CV profiles.

Two pairs of characteristic redox peaks assigned to the multi-step process of Zn²⁺ insertion/extraction were observed, which is similar to the result of the AE (shown in **Figure S26**). Furthermore, the electrode reaction kinetics was investigated by the following equation (4).

$$i = av^b \quad (4)$$

in which *i* is the peak current, *v* is the scan rate, *a* is a coefficient, and *b* is the diffusion-determining coefficient.⁴ The obtained *b* values for both the reduction and oxidation peaks were close to 0.5, indicating a diffusion-controlled behavior which was consistent with the results of the previously reported CVO.²

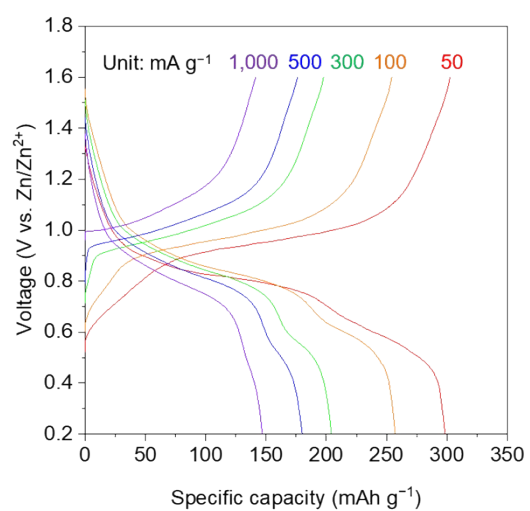


Figure S28. Galvanostatic charge/discharge profiles of the Zn||CVO cell with the BLE at various current densities.

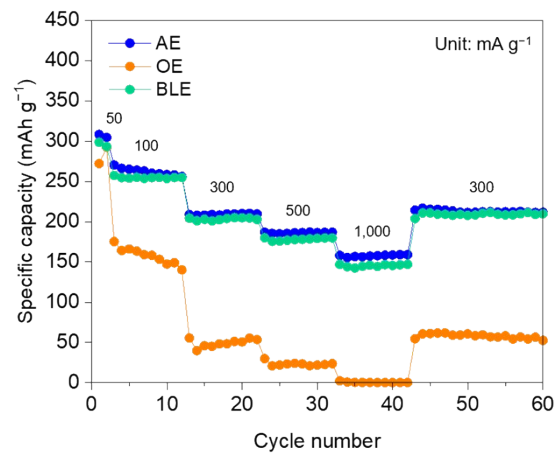


Figure S29. Rate performance of the Zn||CVO cells with the AE, OE, and BLE.

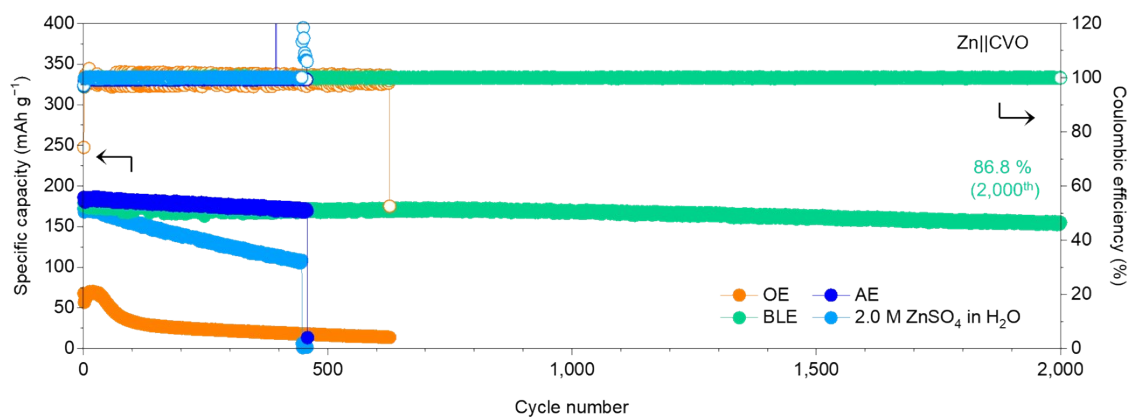


Figure S30. Galvanostatic cycling performance of Zn||CVO cells with 2.0 M ZnSO₄ in H₂O and the BLE at a current density of 300 mA g⁻¹.

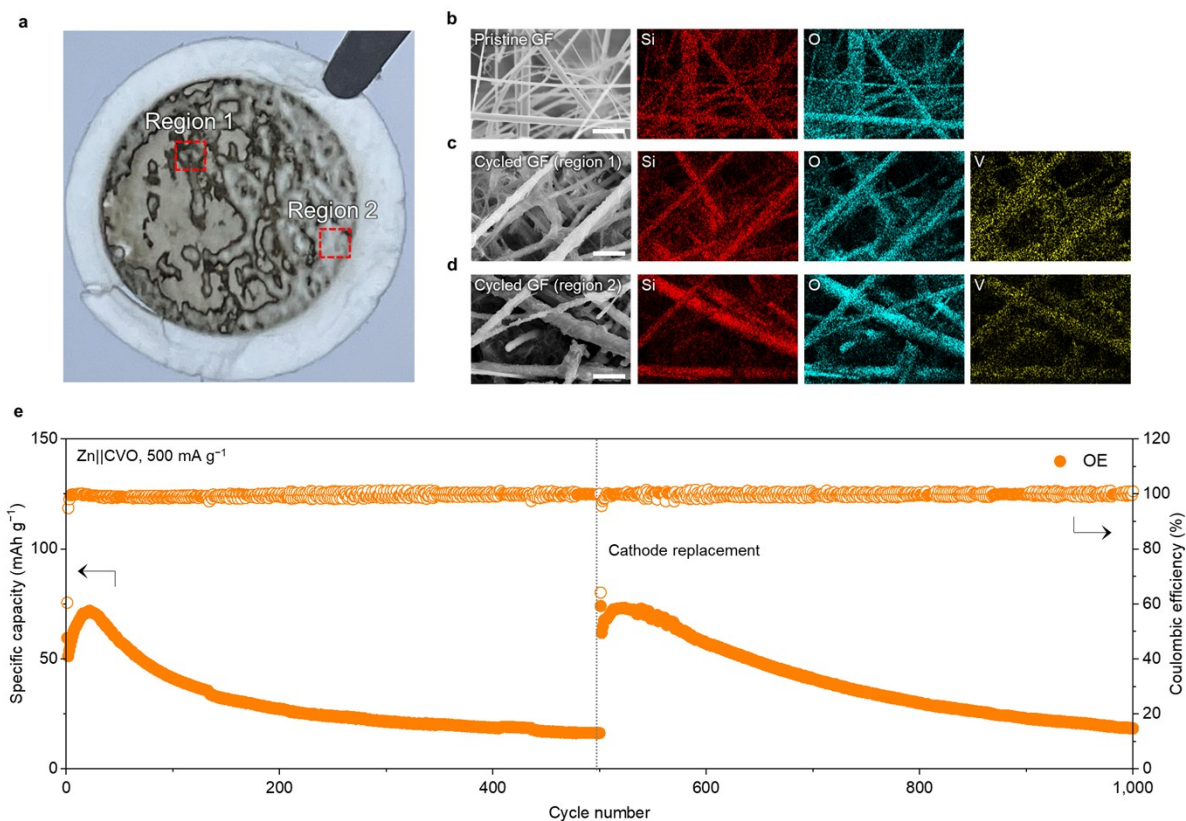


Figure S31. (a) Photograph of the glass microfiber separator (GF) facing the CVO cathode after 500 cycles. (b–d) SEM and EDS elemental mapping images of the glass microfiber separator before (b) and after 500 cycles (c) and (d). (e) Galvanostatic cycling performance of Zn||CVO full cells with OE at a current density of 500 mA g^{-1} . The cycled CVO cathode (after 500 cycles) was replaced by a fresh CVO cathode.

After 500 cycles, the glass microfiber separator facing the CVO cathode was severely contaminated (**Figure S31a**). The SEM and energy dispersive X-ray spectroscopy (EDS) images (**Figure S31b–d**) showed that vanadium is randomly distributed on the surface of the separator, indicating that vanadium ions are dissolved from the CVO cathode during the charge/discharge cycling. Eventually, this undesired dissolution of vanadium ions could induce the capacity decay. The similar results were often reported in previous studies on vanadium oxide-based cathodes.⁵ As additional evidence to verify the structural instability of the CVO during the cycling test, the cycled CVO cathode (after 500 cycles) was replaced by a new CVO cathode using the procedure described in previous studies.⁶ The discharge capacity of the cell reassembled with a fresh CVO cathode was returned to an initial value (**Figure S31e**). These results that the capacity decay of the cell is attributed to the structural instability of the CVO cathode in contact with the OE.

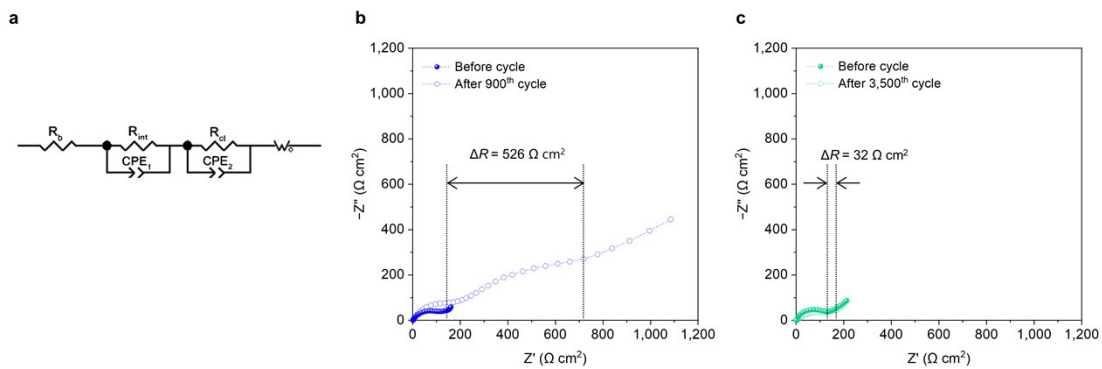


Figure S32. (a) Equivalent circuit of Zn||CVO cells. (b and c) EIS spectra of Zn||CVO cells with 2.0 M ZnSO₄ in H₂O after the 900th cycle (b) and BLE after the 3,500th cycle (c).

The cell with the BLE showed negligible increase in the cell impedance, in comparison to the control cell with the 2.0 M ZnSO₄ aqueous electrolyte showing significant increase in the cell impedance just after 900 cycles.

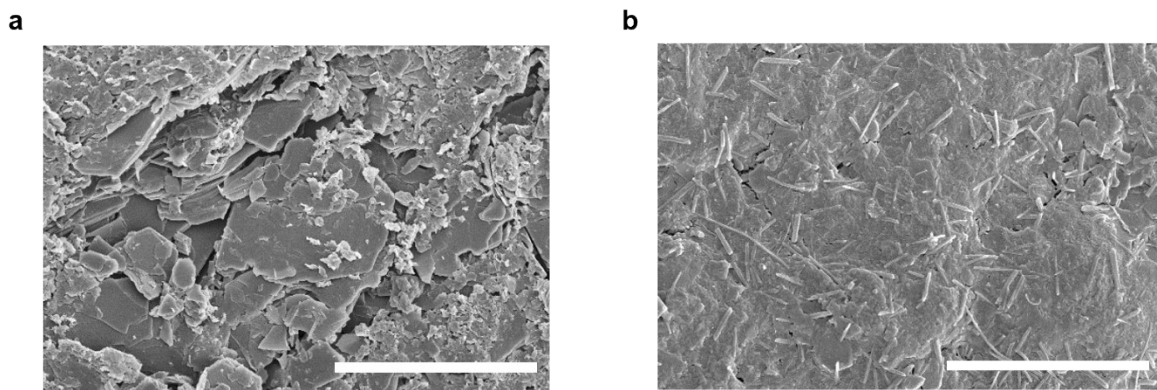


Figure S33. SEM images of cycled Zn in (a) 2.0 M ZnSO₄ in H₂O after the 900th cycle and (b) BLE after 3,500th cycles. Scale bar, 10 μm.

The Zn anode after 900 cycles in the 2.0 M ZnSO₄ aqueous electrolyte showed an uneven porous structure with dendritic Zn growth. By comparison, the Zn anode cycled in the BLE remained smooth and almost unaffected after 3,500 cycles.

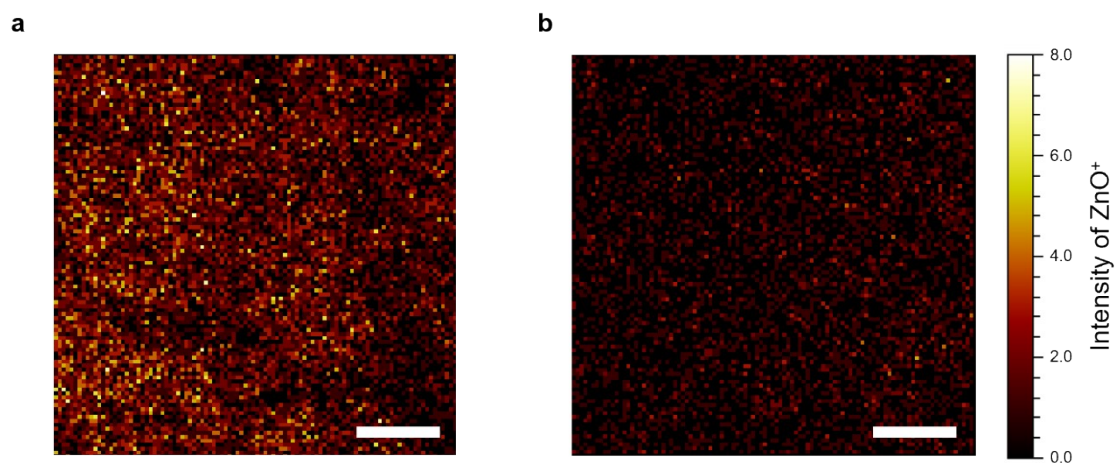


Figure S34. TOF-SIMS images of the distribution of ZnO byproducts formed on the cycled Zn anodes in (a) 2.0 M ZnSO₄ in H₂O after the 900th cycle and (b) BLE after 3,500th cycles. Scale bar, 100 μm.

The distribution of oxidized Zn species on the surface of the cycled Zn anodes was characterized. The Zn anode cycled in the 2.0 M ZnSO₄ aqueous electrolyte showed a high intensity of randomly distributed byproducts such as ZnO⁺ ions. In contrast, the formation of ZnO⁺ ions were remarkably suppressed on the Zn anode cycled in the BLE.

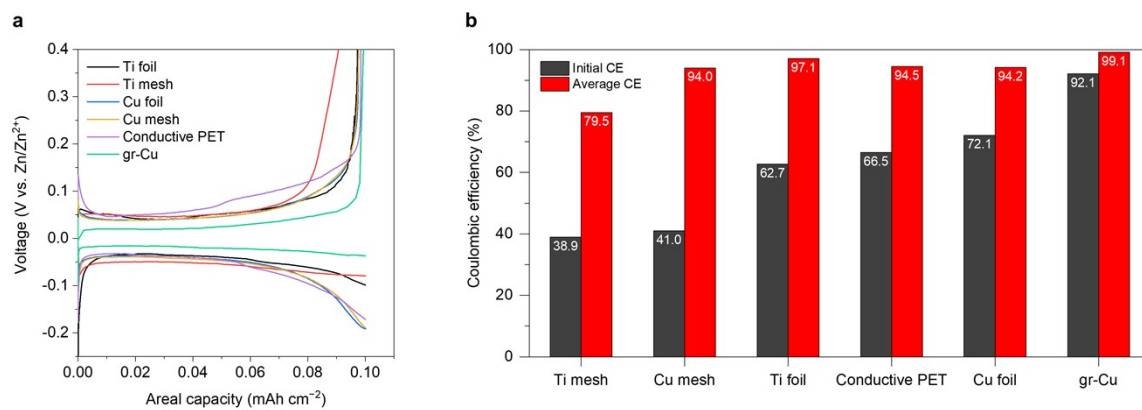


Figure S35. (a) Galvanostatic Zn plating/stripping profiles of Zn||current collectors (e.g., Ti mesh, Cu mesh, Ti foil, conductive PET (polyethylene terephthalate), Cu foil, and gr-Cu) cells at the 30th cycle. (b) Initial CE and average CE (2nd ~ 30th cycles) of Zn|| current collector cells at a current density of 0.1 mA cm⁻² and an areal capacity of 0.1 mAh cm⁻².

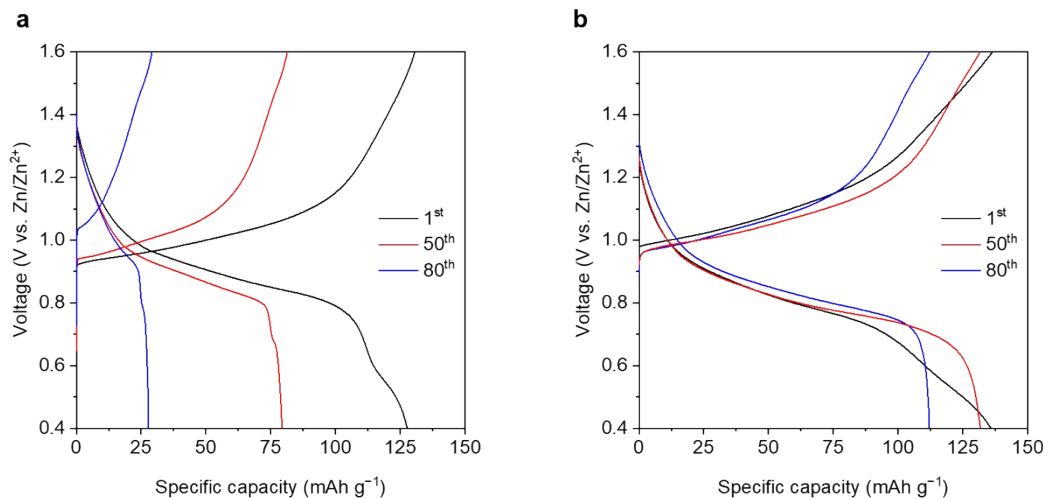


Figure S36. Galvanostatic charge/discharge profiles of the Zn anode-free full cell with (a) 2.0 M ZnSO₄ in H₂O and (b) the BLE.

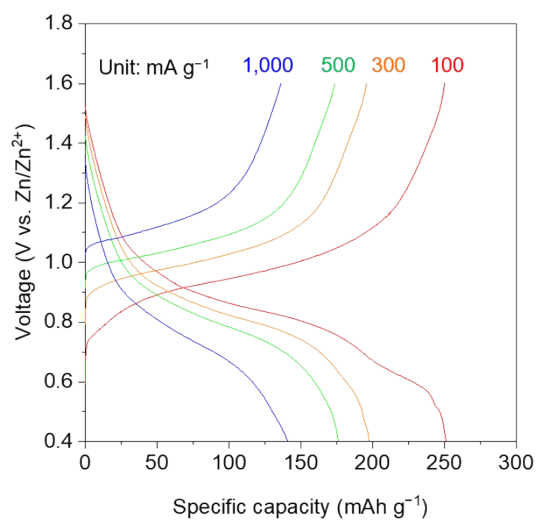


Figure S37. Galvanostatic charge/discharge profiles of the Zn anode-free full cell with the BLE at various current densities.

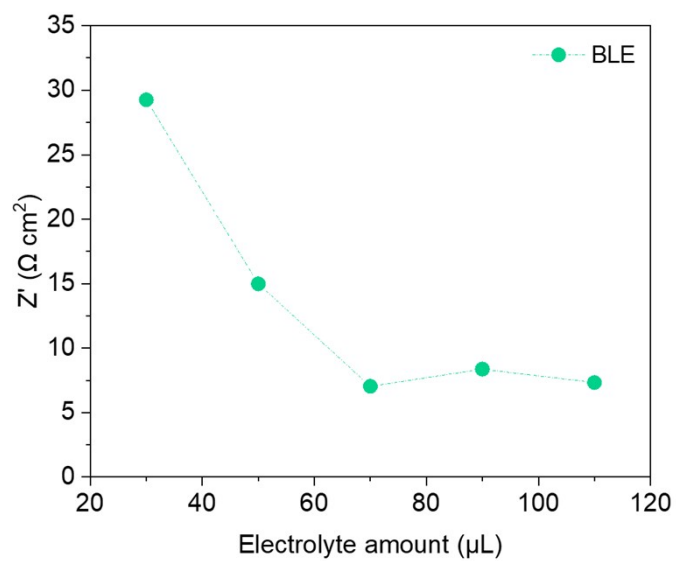


Figure S38. Change in the bulk resistance (R_b) of the Zn||CVO cell (CR2032 coin cell) measured by the EIS analysis as a function of electrolyte amount.

Supplementary Tables

Table S1. Details of MD simulation systems for single-phase electrolytes

	Number of H ₂ O molecules	Number of Zn ²⁺ ions	Number of anions	Initial cell parameter (nm ³)
0.5 m Zn(TFSI) ₂ in H ₂ O	2,220	20	40	4.24 × 4.24 × 4.24
0.5 m Zn(OTf) ₂ in H ₂ O	2,220	20	40	4.15 × 4.15 × 4.15
0.5 m Zn(OAc) ₂ in H ₂ O	2,220	20	40	4.04 × 4.04 × 4.04
1.0 m ZnSO ₄ in H ₂ O	2,220	40	40	4.06 × 4.06 × 4.06
2.0 m ZnSO ₄ in H ₂ O	2,220	80	80	4.03 × 4.03 × 4.03
3.4 m ZnSO ₄ in H ₂ O	2,220	136	136	4.05 × 4.05 × 4.05

Table S2. Details of MD simulation for anion effect toward AN (DEE)/aqueous electrolyte system

Component 1	Component 2	Number of solvent molecules in component 1	Number of solvent molecules in component 2	Number of Zn ²⁺ ions	Number of anions	Initial cell parameter (nm ³)
1.0 m Zn(TFSI) ₂ in H ₂ O	AN	2,220	1050	40	80	4.49 × 4.49 × 8.88
H ₂ O	AN	2,220	775	–	–	4.07 × 4.07 × 8.13
0.5 m Zn(OAc) ₂ in H ₂ O	AN	2,220	775	20	40	4.10 × 4.10 × 8.17
1.0 m ZnSO ₄ in H ₂ O	AN	2,220	775	40	40	4.07 × 4.07 × 8.14
2.0 m ZnSO ₄ in H ₂ O	AN	2,220	775	80	80	4.07 × 4.07 × 8.13
3.4 m ZnSO ₄ in H ₂ O	AN	2,220	775	136	136	4.07 × 4.07 × 8.14
H ₂ O	DEE	2,220	385	–	–	4.06 × 4.06 × 8.10
0.5 m Zn(OTf) ₂ in H ₂ O	DEE	2,220	410	20	40	4.14 × 4.14 × 8.25
0.5 m Zn(TFSI) ₂ in H ₂ O	DEE	2,220	440	20	40	4.23 × 4.23 × 8.46
0.75 m Zn(TFSI) ₂ in H ₂ O	DEE	2,220	465	30	60	4.31 × 4.31 × 8.59
1.0 m Zn(TFSI) ₂ in H ₂ O	DEE	2,220	525	40	80	4.46 × 4.46 × 8.85

Table S3. Details of MD simulation comparing solvent mixture (H₂O/AN) and electrolyte mixture (3.4 m ZnSO₄ in H₂O/0.5 m Zn(TFSI)₂ in AN) system.

Component 1	Component 2	Number of solvent molecules in component 1	Number of solvent molecules in component 2	Number of Zn ²⁺ ions	Number of anions	Initial cell parameter (nm ³)
H ₂ O	AN	4,219	1481	-	-	5.04 × 5.04 × 10.08
3.4 m ZnSO ₄ in H ₂ O	0.5 m Zn(TFSI) ₂ in AN	4,244	1364	260 / 28	260 / 56	5.05 × 5.05 × 10.10

Table S4. Comparison of the ionic conductivity between the BLE and previously reported biphasic electrolytes. N/A (not available) indicates no experimental data in the references.

Ref.	Ionic conductivity (mS cm ⁻¹)		
	Cathode-side electrolyte	Anode-side electrolyte	Biphasic electrolyte
This work	46.8 (3.4 m ZnSO ₄ in H ₂ O)	30.9 (0.5 m Zn(TFSI) ₂ in AN)	37.0
7	N/A (1 M LiTFSI in DMSO)	~6.2 (1 M LiTFSI in PFTOS)	N/A
8	4.77 (0.5 M PTZs in 0.5 M TBAPF ₆ /CH ₂ Cl ₂)	N/A (0.5 M ZnSO ₄ + 0.3 M KPF ₆ in H ₂ O)	N/A
9	6.7 (Organic-rich phase of the mixture)	N/A (Aqueous-rich phase of the mixture)	N/A (0.18 g TEMPO + 2.0 g TEGDME + 0.74 g LiTFSI + 6.0 g H ₂ O + 0.72 g ZnSO ₄ 7H ₂ O + 1.08 g MgSO ₄ + 0.5 g Zn)
10	N/A (1 M LiTFSI in EMS/ETPTA/Al ₂ O ₃)	N/A (2.3 M LiTFSI in TEGDME /ETPTA/Al ₂ O ₃)	~0.5
11	1.23 (1 M LiTFSI in TEGDME)	N/A (1 M LiTFSI in NFTOS)	0.96
12	35.9 (1 M Zn(TFSI) ₂ in H ₂ O)	1.1 (1 M Zn(TFSI) ₂ in TFEP)	N/A
13	8.3 (21 M LiTFSI + 7 M LiOTf)	0.3 (1 M LiTFSI in Pyr ₁₃ TFSI)	0.46

Abbreviations: Acetonitrile (AN), dimethyl sulfoxide (DMSO), perfluorooctyltrimethoxysilane (PFTOS), phenothiazins (PTZs), tetrabutylammonium hexafluorophosphate (TBAPF₆), 2,2,6,6-tetramethylpiperidine (TEMPO), tetraethylene glycol dimethyl ether (TEGDME), ethyl methyl sulfone (EMS), ethoxylated trimethylolpropane triacrylate (ETPTA), nonafluoro-1,1,2,2-tetrahydrohexyltrimethoxysilane (NFTOS), tris(2,2,2-trifluoroethyl)phosphate (TFEP), N-propyl-N-methylpyrrolidinium bis(trifluoromethanesulfonyl)imide (Pyr₁₃TFSI).

Table S5. Experimentally measured ionic conductivities of OE, AE, BLE and hypothetical ionic conductivity of BLE that assumes no resistance at interface.

Temperature (K)	Ionic conductivity (mS cm ⁻¹)			
	OE (σ_1 , experiment)	AE (σ_2 , experiment)	BLE (σ_3 , experiment)	BLE (σ_4 , theoretical if $R_i = 0$)
298.15	30.9	46.8	37.0	37.3
303.15	32.3	53.5	39.6	40.3
323.15	34.9	67.8	45.8	46.0
333.15	37.7	82.9	51.7	51.8

Table S6. Calculation of Zn²⁺ ion diffusion coefficients of the CVO cathodes as a function of DOD.

Electrolyte	DOD (%)	$\Delta\tau$ (s)	M_B (g mol ⁻¹)	V_M (cm ³ mol ⁻¹)	$m_B S^{-1}$ (g cm ⁻²)	ΔE_s (V)	ΔE_τ (V)	$D_{Zn^{2+}}$ (cm ² s ⁻¹)
AE	5.2	3,600	655.76	262.304	0.00246	0.1439	0.1749	2.31E-10
	20.8	3,600	655.76	262.304	0.00246	0.0199	0.0265	1.94E-10
	38.9	3,600	655.76	262.304	0.00246	0.0053	0.0123	6.37E-11
	59.7	3,600	655.76	262.304	0.00246	0.0083	0.0409	1.41E-11
	90.8	3,600	655.76	262.304	0.00246	0.0127	0.0816	8.23E-11
OE	8.0	3,600	655.76	262.304	0.00246	0.0862	0.1835	7.54E-11
	20.1	3,600	655.76	262.304	0.00246	0.0345	0.1052	3.67E-11
	40.2	3,600	655.76	262.304	0.00246	0.0132	0.0797	9.34E-12
	60.2	3,600	655.76	262.304	0.00246	0.0056	0.0880	1.40E-12
	88.3	3,600	655.76	262.304	0.00246	0.0164	0.1810	2.18E-12

The diffusion coefficients were calculated based on the following equation (5).¹⁴

$$D_{Zn^{2+}} = \frac{4}{\pi\Delta\tau} \left(\frac{m_B V_M}{M_B S} \right) \left(\frac{\Delta E_s}{\Delta E_\tau} \right)^2 \quad (5)$$

where m_B is assigned to the mass of the CVO, V_M is the molar volume of the CVO, M_B is the molar mass of the CVO, S is the geometric area of the electrode, ΔE_τ is the voltage change during the single GITT step, ΔE_s is the overall cell voltage change during the constant current step and $\Delta\tau$ is assigned to the duration time of current pulse from GITT profiles shown above.

Table S7. Comparison between the BLE and previously reported Zn anode-free full cells.

Strategy	Positive electrode	Negative electrode	Electrolyte	Specific capacity (mAh g ⁻¹)	Capacity retention / cycle number	Mass loading (mg cm ⁻²)	Ref.
Biphasic electrolyte	Zn_xCVO	gr-Cu	BLE	251.2 (at 100 mA g⁻¹) 197.8 (at 300 mA g⁻¹) 176.2 (at 500 mA g⁻¹) 140.9 (at 1,000 mA g⁻¹)	80.8 % / 90th 76.7 % / 100th (at 1,000 mA g⁻¹)	2.5–3.0	This work
Current collector design	Pre-zincified MnO ₂	C/Cu	3 M Zn(OTf) ₂ + 0.1 M Mn(OTf) ₂	~ 200 (at 1 mA cm ⁻²)	68.2 % / 80 th (at 1 mA cm ⁻²)	–	15
Electrolyte additive	LiMn ₂ O ₄	Stainless steel	2 M ZnSO ₄ + 0.08 M ZnF ₂	91.4 (at 100 mA g ⁻¹) 77.3 (at 200 mA g ⁻¹) 63.2 (at 500 mA g ⁻¹) 54.5 (at 800 mA g ⁻¹) 49.5 (at 1,000 mA g ⁻¹)	75.6 % / 100 th (at 200 mA g ⁻¹)	1.2–1.5	16
Electrolyte additive	Zn _x VOPO ₄	Ti foil	4 m Zn(OTf) ₂ + 0.5 m Me ₃ EtNOTF	~ 135 (at 0.5 mA cm ⁻²)	> 80 % / 90 th (at 0.5 mA cm ⁻²)	~ 3	17

Table S8. Comparison of energy density/power density with previously reported Zn anode-free full cells and Zn-ion batteries

Configuration	Strategy	Positive electrode	Negative electrode	Electrolyte	Energy density (Wh kg ⁻¹)	Power density (W kg ⁻¹)	Ref.
Zn anode-free full cells	Biphasic electrolyte	Zn_xCVO	gr-Cu	BLE	183	73	This work
					140	213	
					119	338	
					87	618	
					Additive	Zn _x VOPO ₄	
Zn-ion full cells	Intercalated anode	ZnMn ₂ O ₄	Na _{0.14} TiS ₂	2 M Zn(OTf) ₂	174	33	18
		Zn _{0.2} MnO ₂	h-MoO ₃	1 M ZnSO ₄	108	61	19
Zn-metal full cells	Electrolyte design	Zn ₂ (OH)VO ₄	Zn	2 M ZnSO ₄ based gel	140	70	20
		Graphene	Zn	WSOE ₄₅ -1	109	150	21
		ZnMn ₂ O ₄ @C	Zn	3 M Zn(OTf) ₂	70	23	22
	Structure modification	NVPF@C	Zn@C	8 M NaClO ₄ + 0.4 M Zn(OTf) ₂	71	166	23
		AC	Zn@ZIF-800	2 M ZnSO ₄	141	70	24
		MnO ₂	Zn@CNT	PVA-LiCl-ZnCl-MnSO ₄ gel	65	126	25
Coating	NH ₄ V ₄ O ₁₀	Glue-coated Zn	3 M Zn(OTf) ₂	190	48	26	

Supplementary Notes

Note S1. Descriptions of molecular dynamics simulation procedures

In this manuscript, different MD simulation procedures and analysis for various types of MD systems were performed for different purposes. Thus, MD simulation procedures are described in **Notes S2–S5**, categorized by their purposes. Note that settings for MD simulation can be found in the **METHOD** section.

Note S2. MD simulations for single-phase electrolytes

To calculate the hydration structure of anions and water structure with varying anions at single-phase aqueous electrolytes, MD simulation was conducted via a three-step procedure. First, the preparation of each system was performed, and the equilibration run was subsequently conducted. Each system was packed with 2220 solvent molecules and the number of salt molecules corresponding to experimental concentration, in three-dimensional periodic cubic simulation box. The details of each model system are summarized in **Table S1**. Geometry optimization was then carried out via steepest-descent algorithm, until the convergence criteria (maximum force below $10 \text{ kJ mol}^{-1} \text{ nm}^{-1}$) was reached. After that, equilibration MD run were conducted sequentially at 298 K with canonical ensemble (i.e., NVT) and at 1 bar and 298 K with the isothermal-isobaric ensemble (i.e., NPT) for 500 ps and 10 ns each. The equilibration of each bulk phase was confirmed by convergence of system density. From the last 2 ns of each calculated trajectory, interaction energy between ions and water molecules, H-bond number, and H-bond distance distribution were obtained. Solubility parameter δ was calculated from the following equations (6) and (7).

$$\delta = \sqrt{\frac{E_{coh}}{V_m}} = \sqrt{\frac{\Delta H_{vap} - RT}{V_m}} \quad (6)$$

$$\Delta H_{vap} = (E_{pot}(g) - k_B T) - E_{pot}(l) \quad (7)$$

Where E_{coh} is the cohesive energy of the system, ΔH_{vap} is heat of vaporization, V_m is molar volume, $E_{pot}(g)$ is the system's potential energy in gas phase, $E_{pot}(l)$ is the system's potential energy in the liquid state, k_B is the Boltzmann's constant and T is absolute temperature.

Note S3. MD simulations for anion effect toward AN/DEE-aqueous electrolyte system

The details of each model system are summarized in **Table S3**. Before constructing the biphasic system, we prepared the equilibrated configuration of the bulk phase of each biphasic system components following a three-step procedure, as described in **Note S2**. Then, initial model of AN/DEE-aqueous electrolyte system was constructed by placing the equilibrated bulk phases in contact, along the z-direction. For these systems, geometry optimization was carried out initially, and equilibration MD run were conducted sequentially at 298 K with canonical ensemble (i.e., NVT) and at 1 bar and 298 K with the isothermal-isobaric ensemble (i.e., NPT) for 500 ps and 5 ns each. To quantify the miscibility of solvents, the non-bonded interaction energy (ΔE_{int}) between water and AN molecules were calculated.

Note S4. MD simulations to compare solvent mixture (H₂O/AN) and electrolyte mixture (3.4 m ZnSO₄ in H₂O/0.5 m Zn(TFSI)₂ in AN) system

The details of each model system are summarized in **Table S4**. As described in **Note S3**, first we prepared the equilibrated bulk phase system and constructed biphasic system. For these systems, geometry optimization was carried out initially, and equilibration MD run were conducted sequentially at 298 K with canonical ensemble (i.e., NVT) and at 1 bar and 298 K with the isothermal-isobaric ensemble (i.e., NPT) for 500 ps and 50 ns each. To quantify the phase-separation behavior of the system, we have calculated ΔE_{int} and demixing index (χ_{demix}). χ_{demix} was calculated using the following equations (8)–(10).

$$\chi_{\text{demix}} = \frac{1}{N} \langle d_i \rangle \quad (8)$$

$$\frac{1}{d_i} = \frac{1}{d_{H_2O,i}} + \frac{1}{d_{AN,i}} \quad (\text{i.e., solvent mixture, } i \text{ ranges from 1 to } n) \quad (9)$$

$$\frac{1}{d_i} = \frac{1}{d_{3.4 \text{ m ZnSO}_4 \text{ in H}_2\text{O},i}} + \frac{1}{d_{0.5 \text{ m Zn(TFSI)}_2 \text{ in AN},i}} \quad (\text{i.e., electrolyte mixture, } i \text{ ranges from 1 to } n) \quad (10)$$

Where n means the number of bins dividing the simulation system equally in the z-direction, N is the normalization factor, d_i is the number density of the system at each bin i , to each solvent and electrolyte. Note that χ_{demix} ranges from 0 to 1, which means totally separate phases and perfectly mixed phase, respectively.

Note S5. MD simulations to calculate Zn²⁺ conduction behavior and free energy profile

To observe ion conduction behavior at BLE system we have applied an electric field on the z-direction of BLE system. The equilibrated BLE system was used as the starting configuration, and we performed an independent simulation applying electric field strength from 0 V nm⁻¹ to 2 V nm⁻¹ with 0.1 V nm⁻¹ increments. The electric field strength of 0.5 V nm⁻¹ was selected to meet the conditions for migrating the Zn²⁺ ions while minimizing the effect on molecular arrangement. In addition, an umbrella sampling simulation was conducted for the equilibrated BLE system. Free energy profiles of Zn²⁺ ion conduction was calculated from the potential of mean force (PMF) using the umbrella sampling method.²⁷⁻²⁹ The starting configurations were generated by moving observed Zn²⁺ ion solvation structure which depends on ion migration path (organic to aqueous phase Zn²⁺(AN)₆), along the z-axis from -2.5 nm to 2.5 nm, with a sampling window of 0.2 nm. Harmonic potential constant for sampling was 750 kJ mol⁻¹ nm⁻². At each sampling window, initial starting configurations are optimized with a position restraint on lithium ion and 20 ns of NVT simulation at 298 K was performed for equilibration and sampling. The last 10 ns trajectories are used for the actual analysis. Analysis was performed via weighted histogram analysis method (WHAM).³⁰

Supplementary References

- 1 H. Li, C. Xu, C. Han, Y. Chen, C. Wei, B. Li and F. Kang, *J. Electrochem. Soc.*, 2015, **162**, A1439.
- 2 Y. Zhang, F. Wan, S. Huang, S. Wang, Z. Niu and J. Chen, *Nat. Commun.* 2020, **11**, 2199.
- 3 T. Brezesinski, J. Wang, S.H. Tolbert and B. Dunn, *Nat. Mater.* 2010, **9**, 146–151.
- 4 F. Wan, L. Zhang, X. Dai, X. Wang, Z. Niu and J.Chen, *Nat. Commun.* 2018, **9**, 1656.
- 5 C. Szczuka, R.-A. Eichel and J. Granwehr, *ACS Appl. Energy Mater.*, 2022, **5**, 449–460.
- 6 X. Ren, L. Zou, X. Cao, M. H. Engelhard, W. Liu, S. D. Burton, H. Lee, C. Niu, B. E. Matthews, Z. Zhu, C. Wang, B. W. Arey, J. Xiao, J. Liu, J.-G. Zhang and W. Xu, *Joule*, 2019, **3**, 1662–1676.
- 7 X. He, X. Liu, Q. Han, P. Zhang, X. Song and Y. Zhao, *Angew. Chem. Int. Ed.*, 2020, **59**, 6397–6405.
- 8 J. Chai, A. Lashgari, A.E. Eisenhart, X. Wang, T.L. Beck and J.J. Jiang, *ACS Materials Lett.*, 2021, **3**, 337–343.
- 9 J. Meng, Q. Tang, L. Zhou, C. Zhao, M. Chen, Y. Shen, J. Zhou, G. Feng, Y. Shen and Y. Huang, *Joule*, 2020, **4**, 953–966.
- 10 S.-J. Cho, G.Y. Jung, S.H. Kim, M. Jang, D.-K. Yang, S.K. Kwak and S.-Y. Lee, *Energy Environ. Sci.*, 2019, **12**, 559–565.
- 11 X. Liu, X. Song, Z. Guo, T. Bian, J. Zhang and Y. Zhao, *Angew. Chem. Int. Ed.*, 2021, **60**, 16360–16365.
- 12 L. Cao, D. Li, T. Deng, Q. Li and C. Wang, *Angew. Chem. Int. Ed.*, 2020, **59**, 19292–19296.
- 13 Y. Qiao, Q. Wang, X. Mu, H. Deng, P. He, J. Yu and H. Zhou, *Joule*, 2019, **3**, 1–16.
- 14 C. Chen, Y. Zhang, Y. Li, Y. Kuang, J. Song, W. Luo, Y. Wang, Y. Yao, G. Pastel, J. Xie, L. Hu, *Adv. Energy Mater.* 2017, **7**, 1700595.
- 15 Y. Zhu, Y. Cui and H. N. Alshareef, *Nano Lett.*, 2021, **21**, 1446–1453.
- 16 Y. An, Y. Tian, K. Zhang, Y. Liu, C. Liu, S. Xiong, J. Feng, Y. Qian, *Adv. Funct. Mater.*, 2021, **31**, 2101886.
- 17 L. Cao, D. Li, T. Pollard, T. Deng, B. Zhang, C. Yang, L. Chen, J. Vatamanu, E. Hu, M.J. Hourwitz, L. Ma, M. Ding, Q. Li, S. Hou, K. Gaskell, J.T. Fourkas, X.-Q. Yang, K. Xu, O. Borodin and C. Wang, *Nat. Nanotechnol.*, 2021, **6**, 902–910.
- 18 Li. Wei, K. Wang, S. Cheng and K. Jiang, *Adv. Energy Mater.* 2019, **9**, 1900993.
- 19 T. Xiong, Y. Zhang, Y. Wang, W.S.V. Lee and J. Xue, *J. Mater. Chem. A* 2020, **8**, 9006.
- 20 D. Chao, C. Zhu, M. Song, P. Liang, X. Zhang, N.H. Tiep, H. Zhao, J. Wang, R. Wang and H. Zhang, *Adv. Mater.* 2018, **30**, 1803181.
- 21 S. Cai, X. Chu, C. Liu, H. Lai, H. Chen, Y. Jiang, F. Guo, Z. Xu, C. Wang and C. Gao, *Adv. Mater.* 2021, **33**, 2007470.
- 22 N. Zhang, F. Cheng, J. Liu, L. Wang, X. Long, X. Liu, F. Li and J. Chen, *Nat. Commun.* 2017, **8**, 405.
- 23 W. Li, K. Wang, M. Zhou, H. Zhan, S. Cheng and K. Jiang, *ACS Appl. Mater. Interfaces* 2018, **10**, 26, 22059.
- 24 Z. Wang, J. Huang, Z. Guo, X. Dong, Y. Liu, Y. Wang and Y. Xia, *Joule*, 2019, **3**, 1289–1300.

- 25 Y. Zeng, X. Zhang, R. Qin, X. Liu, P. Fang, D. Zheng, Y. Tong, X. Lu, *Adv. Mater.* 2019, **31**, 1903675.
- 26 Y. Jiao, F. Li, X. Jin, Q. Lei, L. Li, L. Wang, T. Ye, E. He, J. Wang and H. Chen, *Adv. Funct. Mater.*, 2021, **31**, 2107652.
- 27 G.N. Patey and J.P. Valleau, *Chem. Phys. Lett.* 1973, **21**, 297–300.
- 28 G.M. Torrie and J.P. Valleau, *Chem. Phys. Lett.* 1974, **28**, 578–581.
- 29 G.M. Torrie and J.P. Valleau, *J. Comput. Phys.* 1977, **23**, 187–199.
- 30 S. Kumar, J.M. Rosenberg, D. Bouzida, R.H. Swendsen, P.A. and Kollman, *J. Comput. Chem.* 1992, **13**, 1011–1021.